Volume 26
Number 24
28 June 2024
Pages 16913–17406

PCCP

Physical Chemistry Chemical Physics

rsc.li/pccp

25 YEARS ANNIVERSARY

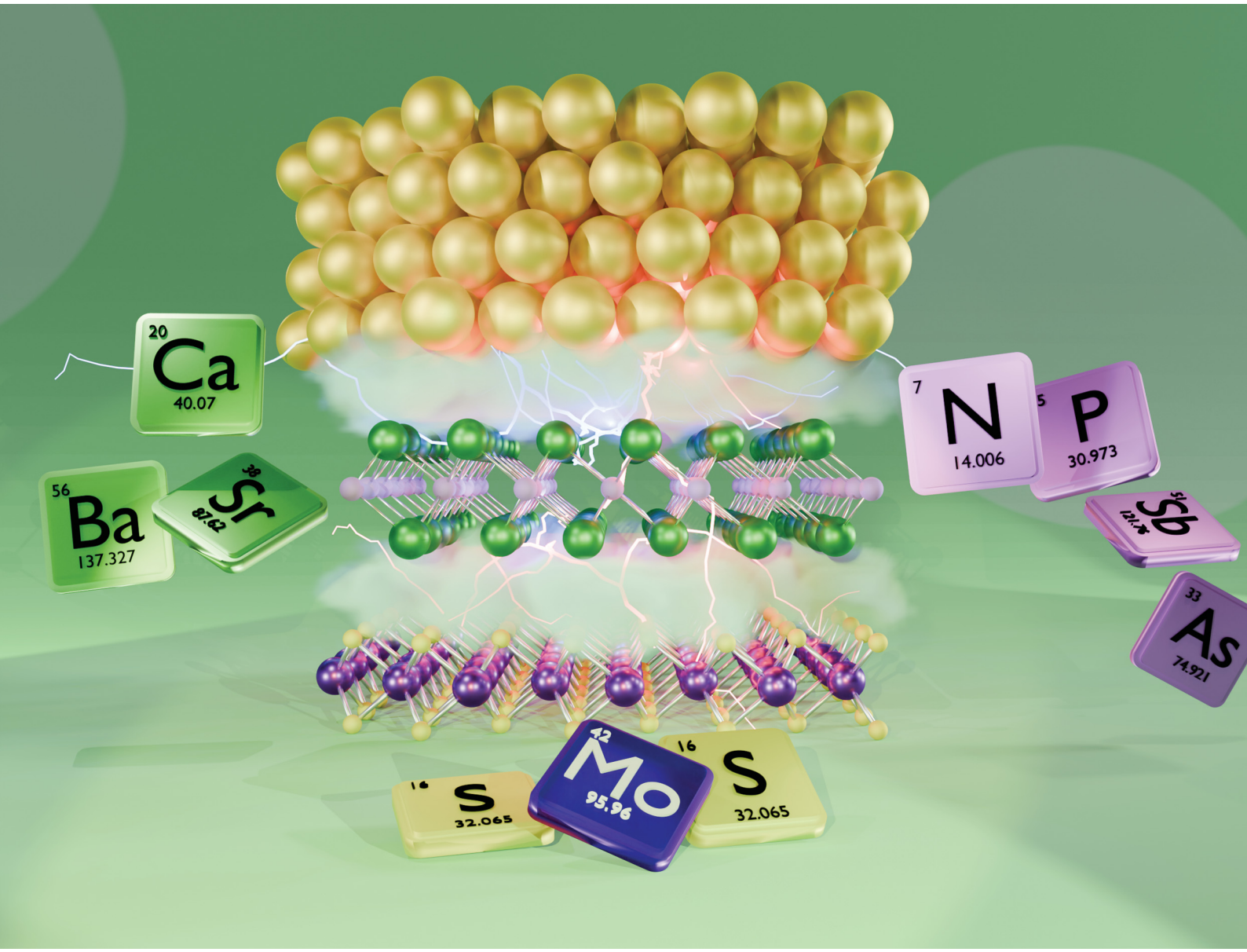

ISSN 1463-9076

ROYAL SOCIETY OF CHEMISTRY

PAPER

Jesse Maassen, Erin R. Johnson *et al.*

Designing barrier-free metal/MoS_2 contacts through electrene insertion

PCCP Owner Societies

PCCP

PAPER

View Article Online
View Journal | View Issue

Cite this: *Phys. Chem. Chem. Phys.*, 2024, **26**, 16947

Designing barrier-free metal/MoS_2 contacts through electrene insertion†

Mohammad Rafiee Diznab, [a] Adrian F. Rumson, [b] Jesse Maassen *[a] and Erin R. Johnson *[ab]

Received 16th December 2023,
Accepted 15th April 2024

DOI: 10.1039/d3cp06112d

rsc.li/pccp

Transition-metal dichalcogenides (TMDCs), including MoS_2, have great potential in electronics applications. However, achieving low-resistance metal contacts is a challenge that impacts their performance in nanodevices due to strong Fermi-level pinning and the presence of a tunnelling barrier. As a solution, we explore a strategy of inserting monolayers of alkaline-earth sub-pnictide electrenes with a general formula of $[M_2X]^+e^-$ (M = Ca, Sr, Ba; X = N, P, As, Sb) between the TMDC and the metal. These electrenes possess two-dimensional sheets of charge on their surfaces that can be readily donated when interfaced with a TMDC semiconductor, thereby lowering its conduction band below the Fermi level and eliminating the Schottky and tunnelling barriers. In this work, density-functional theory (DFT) calculations were performed for metal/electrene/MoS_2 heterojunctions for all stable M_2X electrenes and both Au and Cu metals. To identify the material combinations that provide the most effective Ohmic contact, the charge transfer, band structure, and electrostatic potential were computed. Linear correlations were found between the charge donated to the MoS_2 and both the electrene surface charge and work function. Overall, Ca_2N appears to be the most promising electrene for achieving an Ohmic metal/MoS_2 contact due to its high surface charge density.

1 Introduction

The field of nanoelectronics is poised to undergo a major revolution with the introduction of novel two-dimensional (2D) semiconductor materials. Monolayer transition-metal dichalcogenides (TMDCs) represent a pioneering family of materials in this regard, with MoS_2 serving as their leading member. The stunning features of TMDC-based transistors, such as high mobility,[1] extremely short channel lengths,[2] high on/off ratio,[3] and low sub-threshold swing,[4] make this class of materials well suited for electronic device applications. However, high metal/semiconductor contact resistance has inhibited the efficacy of TMDC-based transistors.[1,5–7] The high contact resistance is primarily caused by (i) the Schottky barrier and Fermi-level pinning, despite the lack of dangling or incomplete bonds on the surface of the TMDC,[8–11] and (ii) the tunnelling barrier caused by the van der Waals (vdW) gap at the metal/TMDC interface.[5,12–14]

The choice of metal plays an important role in the performance of 2D contacts. For some metal/TMDC interfaces, such as Pd/MoS_2, overlap of metal and semiconductor states contributes to electron or hole injection, so that negligible tunnelling barriers are feasible.[6,13] One way to fully overcome the tunnelling barrier is to choose specific metals that can form covalent bonds with the TMDC layer, *e.g.*, Ti when interfaced with MoS_2.[12,15–17] However, such bonding results from strong hybridization of the metal and semiconductor orbitals, which can potentially disrupt the original MoS_2 states and deteriorate the sheet resistivity of the semiconductor.[5,13] That being said, hybridization of the MoS_2 energy bands with the semimetallic materials bismuth and antimony has been demonstrated as one of the best strategies to push the contact resistance towards the quantum limit.[18,19]

Another current strategy to develop practical TMDC-based devices involves introducing an intermediate layer between the metal and 2D semiconductor to address both Fermi-level pinning and tunnelling barrier issues.[9,20–25] One major cause of Fermi-level pinning in 2D metal contacts involving MoS_2 is the production of gap states, mainly of Mo d-orbital character.[11] Based on density-functional theory (DFT) calculations, we previously proposed that the insertion of a Ca_2N monolayer not only removes the Fermi-level pinning, but also eliminates both

[a] *Department of Physics and Atmospheric Science, Dalhousie University, 6310 Coburg Road, Halifax, Nova Scotia, B3H 4R2, Canada. E-mail: jmaassen@dal.ca*
[b] *Department of Chemistry, Dalhousie University, 6243 Alumni Crescent, Halifax, Nova Scotia, B3H 4R2, Canada. E-mail: erin.johnson@dal.ca*

† Electronic supplementary information (ESI) available: Geometric details of all interfaces, computed Bader charge transfer, decomposition of the strain energies, summary of MoS_2 band edges and gaps, results of hybrid DFT calculations on the Ca_2N/MoS_2 interface, and results of WKB calculations. Also included are electronic band structures, DOS, and electrostatic potentials for all studied metal/electrene/MoS_2 interfaces, as well as band structures of the isolated materials at the strained interface geometries. See DOI: https://doi.org/10.1039/d3cp06112d

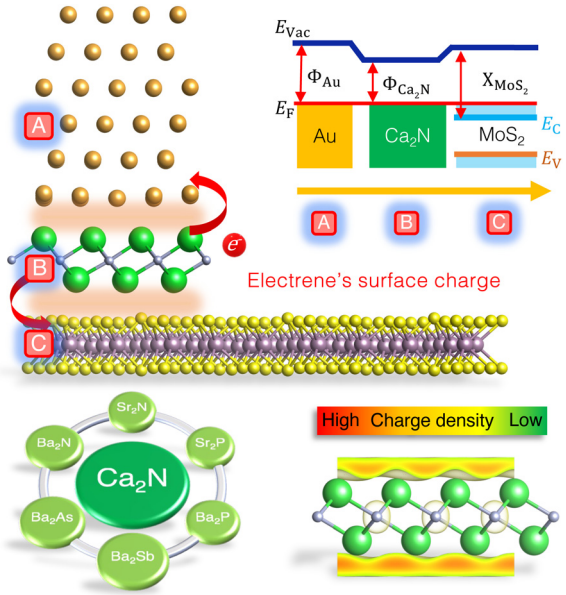

Fig. 1 Top: Schematic design of the Au/MoS_2 interface with monolayer Ca_2N as an intermediate layer. The associated band diagram indicates the removal of the Schottky barrier upon metallization of the MoS_2 bands. Bottom: List of all stable M_2X electrides, along with a 3D representation of the electrene's surface charge.

Schottky and tunnelling barriers, for a model Au/Ca_2N/MoS_2 heterostructure.[20] Fig. 1 (top) shows the atomic configuration and a schematic illustration of the electronic band diagram of a proposed Au/Ca_2N/MoS_2 interface. Here, Φ_{Au} and Φ_{Ca_2N} are the work functions of the metal and the electrene, X_{MoS_2} is the electron affinity of the semiconductor, and E_{vac} and E_F are the vacuum and Fermi levels, respectively. The conduction and valence bands of MoS_2 are also shown as E_c and E_v. Due to charge transfer from the Ca_2N monolayer, the MoS_2 is negatively doped so that its conduction band edge falls below the Fermi level ($E_c < E_F$), removing the Schottky barrier for electron transport.

Ca_2N is a 2D electride;[26,27] this is an ionic material in which the anion is an excess electron that is localized to the interstitial regions between the atomically thin, positively charged, layers of the material. Upon exfoliation, the anionic electrons form delocalized 2D sheets of charge surrounding the surface of the monolayer, now termed an electrene.[28,29] The bottom-right panel of Fig. 1 illustrates the surface charge density of an electrene. These surface states could potentially lead to high charge transport, allowing electrenes to find utility in device applications. Ca_2N is only one member of the family of 2D electrides with a general chemical formula of M_2X (M = Ca, Sr, Ba; X = N, P, As, Sb). The crystal structures of bulk Ca_2N, Sr_2N, and Ba_2N,[27,30] as well as few-layer Ca_2N,[28] have been experimentally characterized, while the others are proposed to be layered electrides on the basis of DFT studies.[28–41] We have previously investigated periodic trends in the electronic, structural, and transport properties of the corresponding monolayer and bilayer electrenes.[42]

In this work, we employ DFT to investigate various electrenes in contact with both Au and Cu metals and MoS_2 to determine which material is the most promising for eliminating the Schottky and tunnelling barriers in metal/MoS_2 contacts. In particular, we determine the extent to which MoS_2 conduction bands become metallized following electrene insertion and analyze the electrostatic potential at the interfaces, which should shed light on electron transport across these contacts. We also identify various correlations between monolayer electride characteristics, such as surface charge densities, and the improved charge transfer and barrier lowering that occurs at the metal/electrene/MoS_2 interfaces.

2 Computational methods

2.1 DFT calculations

All DFT calculations were performed with the Quantum ESPRESSO program,[43,44] using the Perdew–Burke–Ernzerhof (PBE) exchange–correlation functional,[45] the projector augmented-wave (PAW) method,[46,47] and periodic boundary conditions. Dispersion interactions were treated with Grimme's D3BJ pairwise dispersion scheme[48] with Becke–Johnson damping.[49,50] Calculations for all metal/electrene/MoS_2 structures used plane-wave cutoff energies of 80 Ry and 1200 Ry for the wave function and electron density, respectively, and a k-point grid density of $0.03 \times 2\pi$ Å^{-1}. In order to avoid interactions between layers, we adopt a 20 Å vacuum region. The Methfessel–Paxton (MP) smearing method[51] was used to integrate the Brillouin zone with a smearing width of 0.1 eV. Bader charge analysis was performed using the Bader[52–54] code *via* post-processing of the DFT electron density.

2.2 Heterostructure design

After fully relaxing the atomic positions and lattice constants of the isolated MoS_2 monolayer, electrene monolayers, and metal slabs, we employed VASPKIT[55] to build all the metal/MoS_2 and metal/electrene/MoS_2 heterostructures. Two criteria were considered: (i) the MoS_2 layer in all heterostructures is not strained to allow direct comparison between all the interfaces and (ii) the strain on both the electrene layer and the metal slab is under 3.5% for all cases, except for Au/Ba_2Sb/MoS_2, for which there is 4.3% strain for the electrene. Tables S1 and S2 (ESI†) summarize the number of atoms and the in-plane lattice constants for each heterojunction, as well as the percent strains on the electrene and metal slabs. The heterostructure geometries were relaxed with respect to the atomic positions, subject to fixed lattice constants, until the force on each atom was less than 0.1 meV Å^{-1}. Additional geometry relaxations were also performed for the free metal slabs and electrene monolayers using the same lattice constants as the corresponding heterojunctions.

3 Results and discussion

3.1 Exfoliation energies

The structural properties of the studied metal/electrene/MoS_2 heterostructures, including the average interlayer distances, are summarized in Table S2 (ESI†). Overall, the electrene/MoS_2 interlayer distances are found to be smaller than the sum of

the van der Waals radii of the sulfur and alkaline earth metal atoms, taking values of 1.73, 2.41, 2.63, and 2.71 Å, for S, Ca, Sr, and Ba respectively.[56] This reflects the ionic (rather than vdW) nature of these contacts.

To assess the stabilities of the various heterostructures, as well as to quantify the relative importance of strain, ionic binding (from the base density functional), and dispersion interactions, their exfoliation energies were computed. Here, the unstrained exfoliation energy is defined as the energy required to infinitely separate the three materials in the heterojunction:

$$E_{\text{exfo}}^{\text{unstr}} = E_{\text{metal}}^{\text{unstr}} + E_{\text{electrene}}^{\text{unstr}} + E_{\text{MoS}_2} - E_{\text{metal/electrene/MoS}_2}. \quad (1)$$

This involves the energies of the isolated MoS_2 monolayer, electrene monolayer, and metal slab, all at their fully relaxed geometries. As the electrene and metal are strained in the heterostructure, it is reasonable to instead use these strained lattice constants for relaxations of only the atomic positions (and not the lattice constants) of the isolated materials, giving rise to the strained exfoliation energy:

$$E_{\text{exfo}}^{\text{str}} = E_{\text{metal}}^{\text{str}} + E_{\text{electrene}}^{\text{str}} + E_{\text{MoS}_2} - E_{\text{metal/electrene/MoS}_2}. \quad (2)$$

This can be further broken down into contributions from the base density functional and dispersion correction. Finally, the strain energy is

$$E_{\text{strain}} = E_{\text{metal}}^{\text{str}} + E_{\text{electrene}}^{\text{str}} - E_{\text{metal}}^{\text{unstr}} - E_{\text{electrene}}^{\text{unstr}}. \quad (3)$$

The results in Table S3 (ESI†) show that virtually all of the strain energy arises from strain on the metal slab, rather than on the electrene. Note that the MoS_2 layer in all heterostructures is not strained.

The exfoliation energies in Table 1 show that formation of the metal/electrene/MoS_2 interfaces is energetically favourable, and the exfoliation energies are much higher than for the Au/MoS_2 and Cu/MoS_2 interfaces. This is expected due to the high charge transfer from the electrene to the MoS_2 and the metal slab (*vide infra*) resulting in strong ionic bonding, as is evident from the large base-functional contributions to the exfoliation energies (ranging from 49–77% for the strained exfoliation energies). The relative importance of the ionic interactions is largest for the light electrenes (Ca_2N, Sr_2N, and Sr_2P), with the dispersion contributions being more significant for the heavier electrenes containing barium, particularly for Ba_2Sb. From the results in Table 1, we also note that there is generally reduced dispersion binding for Cu as opposed to Au, as expected from the greater atomic size and polarizability of Au. Finally, the strain energies are typically smaller for the Cu interfaces, due to reduced strain on the metal.

Table 1 Total exfoliation energies for metal/electrene/MoS_2 heterostructures. Values were computed using relaxed geometries of the isolated materials with either unstrained (unstr) or strained (str) lattice constants. The strain energies and the decomposition of the strained exfoliation energy into base functional and D3BJ dispersion contributions are also reported. All energies are in meV Å^{-2}, using the area of the strained unit cell

Electrene	None	Ca_2N	Sr_2N	Sr_2P	Ba_2N	Ba_2P	Ba_2As	Ba_2Sb
Au/electrene/MoS_2								
$E_{\text{exfo,unstr}}$	3.5	196.6	181.9	147.0	237.1	169.0	172.0	208.8
E_{strain}	48.2	49.7	47.7	46.6	3.0	46.7	49.5	52.5
$E_{\text{exfo,str}}$	51.7	245.7	229.6	193.6	240.1	215.7	221.5	261.3
$E_{\text{base,str}}$	−7.8	179.5	162.6	144.7	142.2	135.8	132.1	128.5
$E_{\text{disp,str}}$	59.5	66.2	67.0	48.9	97.9	79.9	89.5	132.8
Cu/electrene/MoS_2								
$E_{\text{exfo,unstr}}$	59.8	178.1	198.2	155.5	192.2	151.1	162.8	240.2
E_{strain}	36.7	17.0	8.8	16.3	23.5	35.8	33.9	7.5
$E_{\text{exfo,str}}$	96.5	195.2	207.0	171.8	215.7	187.0	196.8	247.6
$E_{\text{base,str}}$	21.9	145.1	139.3	133.9	127.9	108.5	113.2	122.9
$E_{\text{disp,str}}$	74.6	50.0	83.3	37.9	87.9	78.5	83.6	124.8

As shown in Table 1, all metal/electrene/MoS_2 contacts have much higher binding energies than other high-efficiency 2D TMDC contacts. For example, $PtTe_2$/MoS_2 and graphene/MoS_2 have binding energies of 12.6 meV Å^{-2} and 0.7 meV Å^{-2},[57] respectively. This indicates that the metal/electrene/MoS_2 contact should have higher thermal stability, and the stronger interlayer interactions should promote better charge-carrier injection.

3.2 Bands, densities of states, and charge transfer

Images of the interfaces with inserted electrenes, as well as plots of their electronic band structures, densities of MoS_2 states, and electrostatic potentials, are collected in Fig. S4–S17 (ESI†). We take the two metal/Ca_2N/MoS_2 heterostructures as illustrative examples, with the results shown in Fig. 2. The interface structures are shown in Fig. 2(a) and (e), for Au and Cu, respectively. Panels (b) and (f) show the computed band structures, decomposed according to contributions from each component material. The densities of MoS_2 states are shown in Fig. 2(c) and (g). Integrating the density of MoS_2 states from a particular minimum energy (E_{min}, below which D_{MoS_2} is nearly zero, selected to be −0.5 eV in this work) up to the Fermi energy can reveal the extent of charge doping of the MoS_2 layer (Q_{MoS_2}):

$$Q_{\text{MoS}_2} = \frac{1}{A_{\text{Total}}} \int_{E_{\text{min}}}^{E_{\text{F}}} D_{\text{MoS}_2}(E)\mathrm{d}E, \quad (4)$$

where $D_{\text{MoS}_2}(E)$ is the density of MoS_2 states and A_{Total} is the unit cell area (*i.e.* the total contact area). The integrated part of the DOS is highlighted in light blue in Fig. 2(c). Finally, panels (d) and (h) show the averaged value of the electrostatic potential with respect to the Fermi level, as well as the computed Bader charge transfer upon electrene insertion. The magnified region of Fig. 2(h) shows the tunnelling barrier height (TBH) and tunnelling barrier width (TBW). The TBH is defined as the energy difference between the peak of the averaged electrostatic potential at the interface and the Fermi energy, while the TBW is defined as the distance between the two successive intersections of the averaged potential curve with the Fermi energy.

To understand the changes in electronic structure upon electrene insertion, comparison must be made with data for the the Au/MoS_2 and Cu/MoS_2 interfaces, shown in Fig. S1 (ESI†). These contacts have already been extensively studied

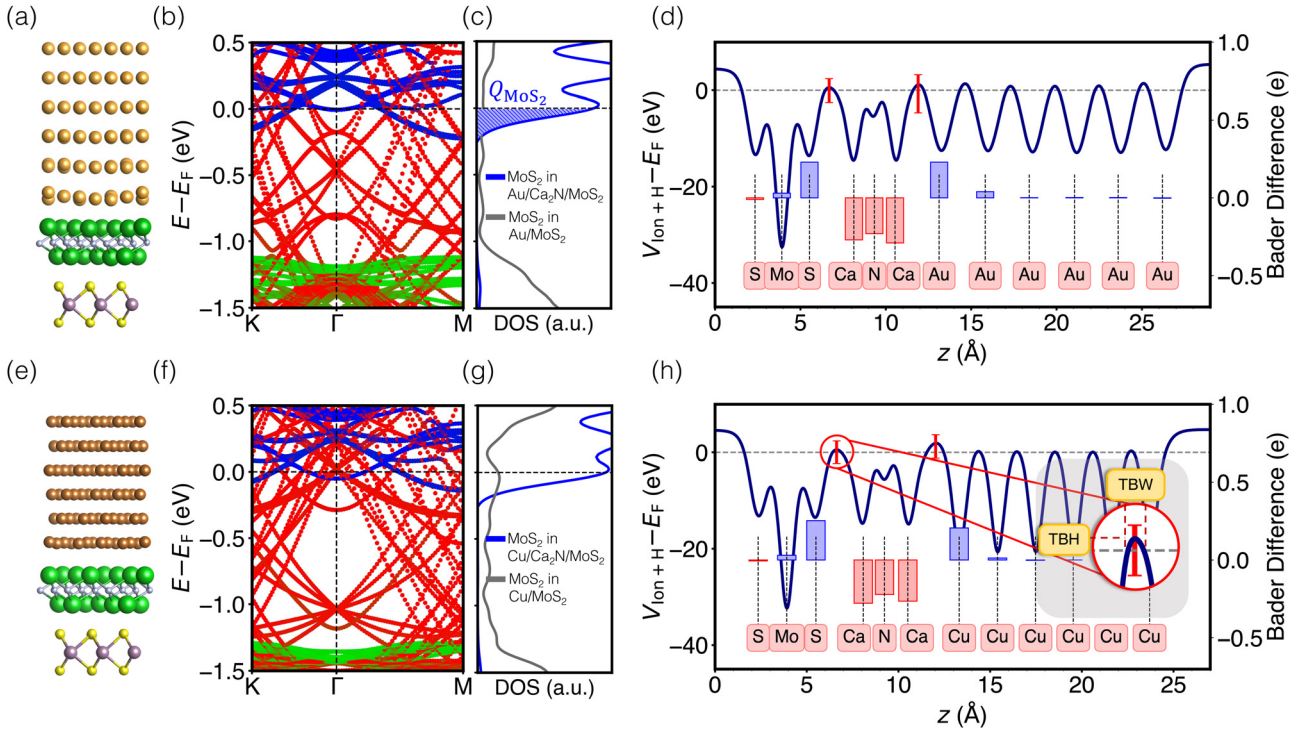

Fig. 2 (a) Optimized structure, (b) material-projected band structure, (c) densities of MoS_2 states per MoS_2 formula unit, and (d) electrostatic potential for the $Au/Ca_2N/MoS_2$ interface. Panels (e)–(h) present the same quantities for the $Cu/Ca_2N/MoS_2$ interface. Metal bands are coloured red, Ca_2N bands are coloured green, and MoS_2 bands are coloured blue. The shaded region of the DOS plot corresponds to Q_{MoS_2}. In the potential plots, the red bars indicate the range of values at the maximum point within the interface regions. The results are overlaid with the differences in Bader atomic charges for the heterostructures, relative to the separated materials. Positive (negative) values indicate accumulation (depletion) of electron density.

using density-functional calculations,[9,11,58,59] so we only briefly discuss some of their most important features. Consistent with previous findings, our results indicate that MoS_2 physisorbs on Au, but chemisorbs on Cu. Carriers at the Au/MoS_2 interface experience a 0.5 eV Schottky barrier and a 3.0 eV tunnelling barrier. For the Cu/MoS_2 interface, electrons that overcome a 0.4 eV Schottky barrier face only a 0.7 eV tunnelling barrier and can travel through some fraction of the interface without tunnelling.

As shown in Fig. 2(b) and (f), Ca_2N insertion shifts the MoS_2 conduction band minimum to −0.2 eV below the Fermi level, meaning that the Schottky barrier is eliminated. This occurs due to electron transfer from the Ca_2N to the MoS_2, which is apparent from comparison with the isolated Ca_2N band structure (Fig. S18–S21, ESI†), as the heterojunction band structures no longer include any Ca_2N surface states near the Fermi level. For both Au- and Cu-based heterojunctions, evaluation of the Bader charges (Table S4, ESI†) shows that *ca.* 0.8 e^- per Ca_2N formula unit is transferred, partially to the metal and partially to the MoS_2. The observation of fractional charge transfer is potentially a consequence of delocalization error,[60,61] which stems from using a generalized gradient approximation (PBE) in this work. Based on a comparison of PBE and HSE06[62] band structures for the bare Ca_2N/MoS_2 interface without any metal (see Fig. S3, ESI†), it is expected that the charge transfer would increase to nearly a full electron per Ca_2N formula unit if hybrid functionals were to be employed. However, this increase in charge transfer is not expected to qualitatively impact our results and, beyond being far too computationally expensive with planewave basis sets to apply to the full metal/electrene/MoS_2 interfaces, hybrid functionals are not recommended for metals.

Overall, the findings discussed for Ca_2N above are general based on our analysis of band structures and Bader charges. For all interfaces considered, electrene insertion at the metal/MoS_2 interfaces results in electron transfer from the electrene to the MoS_2 (see Table S4, ESI†), and a concomitant energy lowering of the MoS_2 conduction band edge (see Table S5, ESI†) to below the Fermi level. Thus, for all metal/electrene/MoS_2 heterostructures, electrene insertion negatively dopes the MoS_2, resulting in the removal of the Schottky barrier and unpinning of the Fermi level with no mid-gap states introduced, as shown in Fig. S4–S17 (ESI†).

In addition to providing a nearly barrierless interface to charge carriers, a good metal contact should also result in minimal distortion of the TMDC states, so as to not deteriorate the semiconductor sheet resistivity. Upon contact formation, the MoS_2 band gap is found to change by up to only ±0.15 eV relative to that of the pristine MoS_2 monolayer (calculated to be 1.72 eV), depending on the choice of the electrene and metal (see Table S5, ESI†). This relatively small modification of the band gap should preserve the resistivity of contacted MoS_2.

3.3 Electrostatic potential profiles and tunneling

While the band structure and DOS plots reveal the promise of the electrene insertion strategy to remove the Schottky barrier, analysis of the electrostatic potential profile of the interface provides information regarding the presence or absence of a tunnelling barrier. Comparison of the Au/Ca_2N/MoS_2 electrostatic potential profile in Fig. 2(d) with the result for the Au/MoS_2 heterojunction in Fig. S1 (ESI†) illustrates how Ca_2N insertion reduces the tunneling barrier at the interface to *ca.* 0.5 eV, compared to *ca.* 3.0 eV for Au/MoS_2 without the electrene. Ca_2N insertion at Cu/MoS_2 leads to a similarly small tunneling barrier of *ca.* 0.5 eV.

In the electrostatic potential plots in Fig. 2(d) and (h), the red bars indicate the range of values (in the x, y plane) that occur at the z position having the highest average potential within the interface regions. The minima of the red bars extend below the Fermi level, indicating Ohmic contact behaviour for some regions of the interface. By projecting the potential profile at the interface into the real-space 2D plane, it is revealed that there is a correlation between the location of the alkaline-earth metal atoms and the Ohmic areas of the interface. For example, for the Au/Ca_2N/MoS_2 heterostructure, the minima of the electrostatic potential occur at the same x, y positions as the calcium sites, while the secondary minima correspond to sulfur locations (see Fig. S4(f), ESI†). This is the case for all metal/electrene/MoS_2 heterostructures considered, as shown in Fig. S4–S17 (ESI†), which allows electrons injected from the metal contact to more easily make their way through to the TMDC.

To ensure that our predictions of high charge transfer and low tunneling barriers are not artifacts of a particular interface geometry, we performed additional calculations for the Cu/Ca_2N/MoS_2 interface, in which the MoS_2 layer was slid over the Ca_2N. Specifically, the MoS_2 layer was shifted uniformly in the a and b cell directions in increments of 0.2, 0.4, 0.6, and 0.8 times the in-plane lattice vectors and the resulting structures geometry optimized. Relative energies, Fermi energies, charge transfer, and Ohmicity fraction (*vide infra*), as well as tunneling barrier heights and widths, are given in Table S6 (ESI†). All show only very minor variations with the fractional sliding coordinate. These results provide confidence that our calculations have used the most stable configurations in terms of MoS_2 sliding, and that our predictions of favourable interface properties are general and not just a feature of one possible geometry.

3.4 Comparison of electrenes

Next, we consider trends involving the extent of charge transfer for all seven electrenes to assess which is the most promising. Fig. 3(a) and (b) show the correlation of Q_{MoS_2} values with the surface charges $\left(Q^{surf}_{M_2X}\right)$ and the work functions (Φ_m) of various monolayer electrenes computed in our previous work.[42] The surface charges of the monolayer electrenes were obtained from the planar average of the integrated local density of states (ILDOS) along the z-axis, integrated over energy from the bottom of the surface bands up to the Fermi level. The averaged ILDOS was then integrated along the z-axis from the outermost metal atom to the vacuum region (where the ILDOS reaches zero) to give $Q^{surf}_{M_2X}$. The almost linear correlation between Q_{MoS_2} and $Q^{surf}_{M_2X}$ indicates that electrenes with higher surface charge densities can donate more charge to the adjacent semiconductor layer.

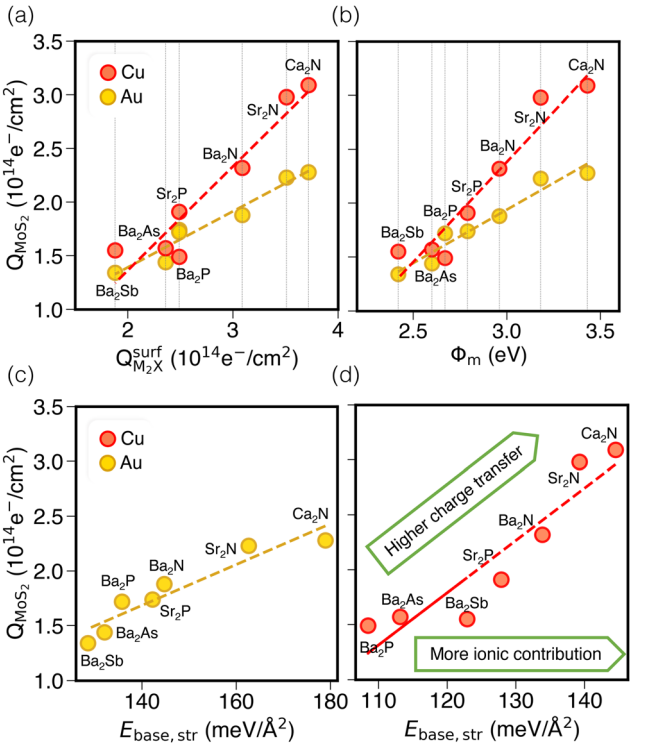

Fig. 3 (a) Correlation of Q_{MoS_2} and $Q^{surf}_{M_2X}$ in Au and Cu-based interfaces. (b) Correlation of Q_{MoS_2} and the monolayer electrene work function (Φ_m). Also shown are correlations between the base-functional (ionic) component of the exfoliation energy and Q_{MoS_2} for Au (c) and Cu (d) interfaces, respectively.

Fig. 3(b) shows a positive correlation between Q_{MoS_2} and the work function, Φ_m, computed[42] for the monolayer electrene. This result is somewhat counterintuitive, since lower work function materials may be expected to promote more electron transfer to the semiconductor. However, we previously found that electrenes with higher work functions have a greater surface charge density[42] (*i.e.* more charge available in the surface states) that is available to donate. Overall, electrenes composed of smaller and chemically harder metal and pnictogen atoms show stronger electrostatic stabilization of the anionic surface charge by the cationic layer. This gives rise to greater surface charge density and tighter binding of the surface states, as quantified by smaller average distances of the surface charge from the alkaline earth metal cations and by larger work functions. Thus, a higher work function implies that the electrene has more charge available to donate to the MoS_2, explaining the greater Q_{MoS_2} values for the corresponding metal/electrene/MoS_2 interfaces.

It should be noted that separate correlations are observed for Au and Cu in Fig. 3(a) and (b) due to the differing

electronegativities of these metals. Since Cu is less electronegative than Au, it will accept less charge. Indeed, the computed Bader charges in Table S4 (ESI†) illustrate that, for any specified electrene, $Q_{Au}^{Bader} > Q_{Cu}^{Bader}$. As a result, more charge is available to be donated to the MoS_2 layer in the case of a Cu surface, such that Q_{MoS_2} values are higher for Cu/electrene/MoS_2 heterostructures compared to their Au counterparts, regardless of the choice of electrene. Hence, the MoS_2 layer receives a greater fraction of the electrene's surface charge when in contact with the less electronegative metal.

By considering only the base-functional contribution, $E_{base,str}$, we can also correlate the ionic (*i.e.* non-dispersion) part of the exfoliation energy and the metallization of the semiconductor (Q_{MoS_2}), as shown in Fig. 3(c) and (d). Strong linear correlations are observed for both Au/electrene/MoS_2 and Cu/electrene/MoS_2 heterostructures. Ca_2N and Sr_2N, which possess the largest electrene surface charge densities, also have the highest ionic contributions to the exfoliation energies for these interfaces. The results are in line with the periodic trend in the exfoliation energies of the corresponding bulk electrides.[42]

Fig. 4 schematically depicts the measures used for assessing contacts in this study, which are also collected in Table S7 (ESI†). Panel (a) shows that the extent of charge transfer, Q_{MoS_2}, is greatest for Ca_2N, followed by Sr_2N and Ba_2N. This is the same trend observed for the monolayer surface charge, as noted above. Values are also shown for the two metal/MoS_2 interfaces for comparison, where there is still a Schottky barrier present

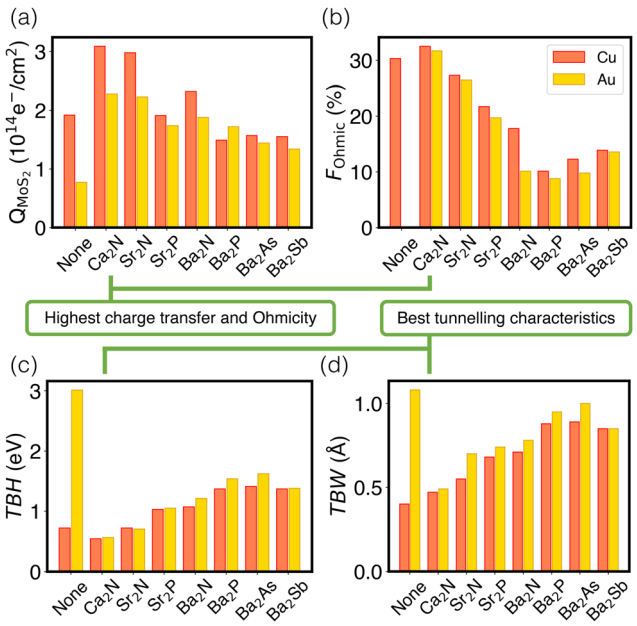

Fig. 4 Bar graphs showing the variation of four figures of merit as a function of the electrene in the metal/electrene/MoS_2 contacts. The individual plots show: (a) the charge transfer to MoS_2, Q_{MoS_2}; (b) the fraction of the contact area that is Ohmic, F_{Ohmic}; (c) the tunneling barrier height, TBH; and (d) tunneling barrier width, TBW. Results for the metal/MoS_2 interfaces with no electrene are shown for comparison; note that the Q_{MoS_2} for these two cases results from mid-gap states rather than from the MoS_2 conduction band.

and the Q_{MoS_2} values quantify the charge occupying mid-gap states up to 0.5 eV below the Fermi level. This is in contrast to the metal/electrene/MoS_2 interfaces, where there are no mid-gap states present and Q_{MoS_2} quantifies the metallization of the MoS_2 conduction band.

The Ohmicity of metal/electrene/MoS_2 contacts can be quantified from analysis of the electrostatic potential at the electrene/MoS_2 interface. The Ohmicity fraction is defined as

$$F_{Ohmic} = \frac{A_{V<E_F}}{A_{Total}}, \quad (5)$$

where $A_{V<E_F}$ and A_{Total} are the barrier-free contact area and total contact area of the interface, respectively. Values of F_{Ohmic} for all metal/electrene/MoS_2 contacts are summarized in Fig. 4(b). Regardless of metal, Ca_2N shows superior contact behaviour in terms of Ohmicity compared to the other electrenes, followed by Sr_2N and Sr_2P. Furthermore, since copper is less electronegative than gold, more charge per formula unit is donated to the MoS_2 layer. This results in greater Q_{MoS_2} and F_{Ohmic} values for the Cu/electrene/MoS_2 contacts, relative to their Au-based counterparts.

Tunnelling characteristics of the contacts are also compared in Fig. 4(c) and (d) for all metal/electrene/MoS_2 configurations. It is imperative that the tunnelling barrier be small enough to maximize the transmission probability. Regardless of the choice of the metal, Ca_2N manifests the lowest TBH and TBW, followed by Sr_2N and Sr_2P. Also, consistent with the F_{Ohmic} results, Cu-based heterostructures show slightly smaller TBWs compared to their Au counterparts. Using the WKB approximation[63] (see Section 4 of the ESI†), the calculated tunnelling specific resistivity of Au/MoS_2 is 1.2×10^{-9} Ω cm^2, with a tunnelling probability of $\leq$1%. As such, insertion of monolayer Ca_2N, which raises the tunneling probability to >20%, lowers the contact resistivity by almost two orders of magnitude. However, since the Cu/MoS_2 tunnelling barrier is negligible, the electrene insertion strategy is most helpful with the elimination of the Schottky barrier in this case. Following the same trends as extracted from the electrostatic potential plots, Ca_2N shows the highest tunnelling probability and lowest tunnelling specific resistivity of all the electrenes considered, followed by Sr_2N.

Finally, it is insightful to compare the metal/electrene/MoS_2 tunnelling characteristics with those of the elemental semimetal contacts of MoS_2, which currently set the gold standard of 2D contacts. For example, Sb(01$\bar{1}$2)/MoS_2 and Sb(0001)/MoS_2 show TBWs of 1.35 Å and 1.39 Å, respectively,[18] whereas the TBWs of {Au,Cu}/Ca_2N/MoS_2 are ~0.5 Å. The tunnelling barrier height of {Au,Cu}/Ca_2N/MoS_2 is also significantly lower than that of Sb(01$\bar{1}$2)/MoS_2 (3.05 eV) and Sb(0001)/MoS_2 (3.13 eV).[18] Our metal/electrene/MoS_2 interfaces also show better tunnelling characteristics than a Bi(0001)/MoS_2 interface with a TBW and TBH of 1.66 Å and 3.6 eV, respectively.[19]

4 Conclusion

To summarize our results, considering all four figures of merit employed (Q_{MoS_2}, F_{Ohmic}, TBW, and TBH), we find that Ca_2N is consistently the most favourable electrene material to insert to

eliminate Schottky and tunnelling barriers across the Au/MoS_2 or Cu/MoS_2 interfaces, owing to its high surface charge density. Sr_2N takes second place for all figures of merit and also appears to be promising, although somewhat less so than Ca_2N. Finally, since Cu is less electronegative than Au, it accepts less charge from the electrene layer, resulting in a more metallized MoS_2, regardless of the choice of electrene. Insertion of electrides appears to be a highly promising strategy to generate n-type (but not p-type) Ohmic contacts since they are excellent reducing agents (but not oxidizing agents). Provided the practical experimental challenges of electrene exfoliation can be overcome,[28] including addressing problems with air and water stability,[64] insertion of 2D electrenes should be a promising approach to improve electron transport across metal/TMDC heterojunctions.

Conflicts of interest

There are no conflicts to declare.

Acknowledgements

This research was supported by the Semiconductor Research Corporation (SRC) and the Digital Research Alliance of Canada.

References

1 S. Das, H.-Y. Chen, A. V. Penumatcha and J. Appenzeller, *Nano Lett.*, 2013, **13**, 100–105.
2 L. Xie, M. Liao, S. Wang, H. Yu, L. Du, J. Tang, J. Zhao, J. Zhang, P. Chen and X. Lu, *et al.*, *Adv. Mater.*, 2017, **29**, 1702522.
3 B. Radisavljevic, A. Radenovic, J. Brivio, V. Giacometti and A. Kis, *Nat. Nanotechnol.*, 2011, **6**, 147–150.
4 X.-F. Wang, H. Tian, Y. Liu, S. Shen, Z. Yan, N. Deng, Y. Yang and T.-L. Ren, *ACS Nano*, 2019, **13**, 2205–2212.
5 A. Allain, J. Kang, K. Banerjee and A. Kis, *Nat. Mater.*, 2015, **14**, 1195–1205.
6 W. Liu, J. Kang, W. Cao, D. Sarkar, Y. Khatami, D. Jena and K. Banerjee, *2013 IEEE Intl. Electron Device Mtg.*, 2013, pp. 19–4.
7 H. Liu, A. T. Neal and P. D. Ye, *ACS Nano*, 2012, **6**, 8563–8569.
8 C. Kim, I. Moon, D. Lee, M. S. Choi, F. Ahmed, S. Nam, Y. Cho, H.-J. Shin, S. Park and W. J. Yoo, *ACS Nano*, 2017, **11**, 1588–1596.
9 M. Farmanbar and G. Brocks, *Phys. Rev. B: Condens. Matter Mater. Phys.*, 2015, **91**, 161304.
10 P. Bampoulis, R. van Bremen, Q. Yao, B. Poelsema, H. J. Zandvliet and K. Sotthewes, *ACS Appl. Mater. Interfaces*, 2017, **9**, 19278–19286.
11 C. Gong, L. Colombo, R. M. Wallace and K. Cho, *Nano Lett.*, 2014, **14**, 1714–1720.
12 I. Popov, G. Seifert and D. Tománek, *Phys. Rev. Lett.*, 2012, **108**, 156802.
13 J. Kang, W. Liu, D. Sarkar, D. Jena and K. Banerjee, *Phys. Rev. X*, 2014, **4**, 031005.
14 T. Shen, J.-C. Ren, X. Liu, S. Li and W. Liu, *J. Am. Chem. Soc.*, 2019, **141**, 3110–3115.
15 K. Stokbro, M. Engelund and A. Blom, *Phys. Rev. B: Condens. Matter Mater. Phys.*, 2012, **85**, 165442.
16 J. Kang, D. Sarkar, W. Liu, D. Jena and K. Banerjee, *2013 IEEE Intl. Electron Device Mtg.*, 2012, pp. 17–4.
17 L.-Y. Gan, Y.-J. Zhao, D. Huang and U. Schwingenschlögl, *Phys. Rev. B: Condens. Matter Mater. Phys.*, 2013, **87**, 245307.
18 W. Li, X. Gong, Z. Yu, L. Ma, W. Sun, S. Gao, Ç. Köroğlu, W. Wang, L. Liu and T. Li, *et al.*, *Nature*, 2023, **613**, 274–279.
19 P.-C. Shen, C. Su, Y. Lin, A.-S. Chou, C.-C. Cheng, J.-H. Park, M.-H. Chiu, A.-Y. Lu, H.-L. Tang and M. M. Tavakoli, *et al.*, *Nature*, 2021, **593**, 211–217.
20 F. Kaadou, J. Maassen and E. R. Johnson, *J. Phys. Chem. C*, 2021, **125**, 11656–11664.
21 Y. Liu, J. Guo, Y. Wu, E. Zhu, N. O. Weiss, Q. He, H. Wu, H.-C. Cheng, Y. Xu and I. Shakir, *et al.*, *Nano Lett.*, 2016, **16**, 6337–6342.
22 H.-J. Chuang, B. Chamlagain, M. Koehler, M. M. Perera, J. Yan, D. Mandrus, D. Tomanek and Z. Zhou, *Nano Lett.*, 2016, **16**, 1896–1902.
23 M. Farmanbar and G. Brocks, *Adv. Electron. Mater.*, 2016, **2**, 1500405.
24 Y. Du, L. Yang, J. Zhang, H. Liu, K. Majumdar, P. D. Kirsch and D. Y. Peide, *IEEE Electron Dev. Lett.*, 2014, **35**, 599–601.
25 W. S. Leong, X. Luo, Y. Li, K. H. Khoo, S. Y. Quek and J. T. Thong, *ACS Nano*, 2015, **9**, 869–877.
26 J. L. Dye, *Acc. Chem. Res.*, 2009, **42**, 1564–1572.
27 K. Lee, S. W. Kim, Y. Toda, S. Matsuishi and H. Hosono, *Nature*, 2013, **494**, 336–340.
28 D. L. Druffel, K. L. Kuntz, A. H. Woomer, F. M. Alcorn, J. Hu, C. L. Donley and S. C. Warren, *J. Am. Chem. Soc.*, 2016, **138**, 16089–16094.
29 D. L. Druffel, A. H. Woomer, K. L. Kuntz, J. T. Pawlik and S. C. Warren, *J. Mater. Chem. C*, 2017, **5**, 11196–11213.
30 G. V. Vajenine, A. Grzechnik, K. Syassen, I. Loa, M. Hanfland and A. Simon, *C. R. Chim*, 2005, **8**, 1897–1905.
31 T. Kocabas, A. Özden, I. Demiroğlu, D. Çakr and C. Sevik, *J. Phys. Chem. Lett.*, 2018, **9**, 4267–4274.
32 S. Guan, S. A. Yang, L. Zhu, J. Hu and Y. Yao, *Sci. Rep.*, 2015, **5**, 1–14.
33 S. G. Dale and E. R. Johnson, *Phys. Chem. Chem. Phys.*, 2017, **19**, 27343–27352.
34 S. Liu, W. Li, S. W. Kim and J.-H. Choi, *J. Phys. Chem. C*, 2019, **124**, 1398–1404.
35 N. E. Brese and M. O'Keeffe, *J. Solid State Chem.*, 1990, **87**, 134–140.
36 T. Inoshita, S. Takemoto, T. Tada and H. Hosono, *Phys. Rev. B*, 2017, **95**, 165430.
37 W. Ming, M. Yoon, M.-H. Du, K. Lee and S. W. Kim, *J. Am. Chem. Soc.*, 2016, **138**, 15336–15344.
38 X.-L. Qiu, J.-F. Zhang, H.-C. Yang, Z.-Y. Lu and K. Liu, *Phys. Rev. B*, 2022, **105**, 165101.
39 P. H. Souza, D. Kuritza, J. E. Padilha and R. H. Miwa, *Phys. Rev. B*, 2022, **105**, 235301.
40 B. Mortazavi, G. R. Berdiyorov, M. Shahrokhi and T. Rabczuk, *J. Alloys Compd.*, 2018, **739**, 643–652.
41 X. Zeng, S. Zhao, Z. Li and J. Yang, *Phys. Rev. B*, 2018, **98**, 155443.

42 M. R. Diznab, E. R. Johnson and J. Maassen, *Nanoscale*, 2023, **15**, 12038–12047.
43 P. Giannozzi, S. Baroni, N. Bonini, M. Calandra, R. Car, C. Cavazzoni, D. Ceresoli, G. L. Chiarotti, M. Cococcioni and I. Dabo, *et al.*, *J. Phys.: Condens. Matter*, 2009, **21**, 395502.
44 P. Giannozzi, O. Andreussi, T. Brumme, O. Bunau, M. B. Nardelli, M. Calandra, R. Car, C. Cavazzoni, D. Ceresoli and M. Cococcioni, *et al.*, *J. Phys.: Condens. Matter*, 2017, **29**, 465901.
45 J. P. Perdew, K. Burke and M. Ernzerhof, *Phys. Rev. Lett.*, 1996, **77**, 3865.
46 P. E. Blöchl, *Phys. Rev. B: Condens. Matter Mater. Phys.*, 1994, **50**, 17953.
47 G. Kresse and D. Joubert, *Phys. Rev. B: Condens. Matter Mater. Phys.*, 1999, **59**, 1758.
48 S. Grimme, J. Antony, S. Ehrlich and H. Krieg, *J. Chem. Phys.*, 2010, **132**, 154104.
49 S. Grimme, S. Ehrlich and L. Goerigk, *J. Comput. Chem.*, 2011, **32**, 1456–1465.
50 E. R. Johnson and A. D. Becke, *J. Chem. Phys.*, 2006, **124**, 174104.
51 M. Methfessel and A. Paxton, *Phys. Rev. B: Condens. Matter Mater. Phys.*, 1989, **40**, 3616.
52 G. Henkelman, A. Arnaldsson and H. Jónsson, *Comput. Mater. Sci.*, 2006, **36**, 354–360.
53 E. Sanville, S. D. Kenny, R. Smith and G. Henkelman, *J. Comput. Chem.*, 2007, **28**, 899–908.
54 W. Tang, E. Sanville and G. Henkelman, *J. Phys.: Condens. Matter*, 2009, **21**, 084204.
55 V. Wang, N. Xu, J.-C. Liu, G. Tang and W.-T. Geng, *Comput. Phys. Commun.*, 2021, **267**, 108033.
56 S. S. Batsanov, *Inorg. Mater.*, 2001, **37**, 871–885.
57 S. Hao, S. Han, J. Zhang, J. Li, N. Wang and X. Li, *ACS Appl. Nano Mater.*, 2023, **6**, 2285–2291.
58 M. Farmanbar and G. Brocks, *Phys. Rev. B*, 2016, **93**, 085304.
59 B. A. Helfrecht, D. M. Guzman, N. Onofrio and A. H. Strachan, *Phys. Rev. Mater.*, 2017, **1**, 034001.
60 K. R. Bryenton, A. A. Adeleke, S. G. Dale and E. R. Johnson, *Wiley Interdiscip. Rev.: Comput. Mol. Sci.*, 2023, **13**, e1631.
61 D. Hait and M. Head-Gordon, *J. Phys. Chem. Lett.*, 2018, **9**, 6280–6288.
62 A. V. Krukau, O. A. Vydrov, A. F. Izmaylov and G. E. Scuseria, *J. Chem. Phys.*, 2006, **125**, 224106.
63 J. G. Simmons, *J. Appl. Phys.*, 1963, **34**, 1793–1803.
64 S. H. Kang, D. Thapa, B. Regmi, S. Ren, Y.-M. Kim, S.-G. Kim and S. W. Kim, *J. Am. Chem. Soc.*, 2022, **144**, 4496–4506.

